Available online at www.sciencedirect.com

ScienceDirect

Proceedings of the Combustion Institute 39 (2023) 5611–5619

Proceedings of the Combustion Institute

www.elsevier.com/locate/proci

High-pressure kinetic interactions between CO and H_2 during syngas catalytic combustion on PdO

Ran Sui [b], John Mantzaras [a,*], Rolf Bombach [c], Meysam Khatoonabadi [a]

[a] *Laboratory for Scientific Computing and Modeling, Paul Scherrer Institute, CH-5232 Villigen, PSI, Switzerland*
[b] *Department of Mechanical and Aerospace Engineering, Missouri University of Science and Technology, Rolla, MO 65409, United States*
[c] *Energy Systems Integration Platform, Paul Scherrer Institute, CH-5232 Villigen, PSI, Switzerland*

Received 2 January 2022; accepted 21 June 2022
Available online 8 July 2022

Abstract

The catalytic combustion of H_2/CO/O_2/N_2 mixtures over PdO was investigated at pressures 3 to 10 bar, H_2:CO volumetric ratios 1:5 to 3:1, and global equivalence ratios $\varphi = 0.13$ and 0.23. The catalyst surface temperatures were controlled to 540–690 K, a range especially important for hybrid hetero-/homogeneous combustion approaches with large gas turbines at idle or part-load operation and for microreactors with recuperative small-scale turbines. In situ Raman measurements determined the major gas-phase species concentrations over the catalyst boundary layers in a channel-flow reactor, thermocouples monitored the surface temperatures, and surface characterization identified the catalyst oxidation state (PdO) and surface morphology. A 2-D CFD code with a detailed catalytic reaction mechanism simulated the experiments. Simulations and measurements of the combustion of the individual fuel components revealed pressure dependencies $\sim p^{0.74}$ and $\sim p^{0.10}$ for the CO and H_2 reactivities, respectively, at the investigated equivalence ratios. In the combustion of H_2/CO blends, transition temperatures (T_{TRAN}) were identified, below (above) which H_2 inhibited (promoted) chemically the oxidation of CO. The transition temperatures decreased with increasing H_2:CO volumetric ratio, pressure, and equivalence ratio. Sensitivity analysis indicated that the H_2 and O_2 adsorption reactions had the larger inhibiting effect on CO oxidation, particularly at lower pressures. Comparisons with other noble metals showed that the PdO transition temperatures were higher than those on Pt and Rh. Even though this behavior favored Pt and Rh for the ignition of syngas in practical catalytic burners, the H_2 and CO kinetic coupling (H_2 inhibition) was considerably weaker on PdO at $T < T_{TRAN}$, thus rendering PdO also potentially suitable for low temperature syngas ignition.

Keywords: High-pressure syngas catalytic combustion on PdO; In situ Raman measurements; Inhibition of CO oxidation by H_2; Transition temperatures in CO oxidation; Pressure effect on CO and H_2 kinetic coupling

* Corresponding author.
E-mail address: ioannis.mantzaras@psi.ch (J. Mantzaras).

https://doi.org/10.1016/j.proci.2022.06.010

1. Introduction

Syngas, a mixture comprising mainly H_2 and CO, is an important renewable energy carrier with a carbon-neutral footprint that allows for increased fuel supply security. Natural-gas-fired Integrated Gasification Combined Cycle (IGCC) large power plants with pre-combustion CO_2 capture, reform the natural gas fuel to syngas and combust the latter [1]. Syngas combustion is also relevant to Solid Oxide Fuel Cell (SOFC) decentralized power systems. To avoid direct use of hydrocarbons that may cause strong carbon deposition and catalyst deactivation of the Ni-based SOFC anodes, the fuel is reformed to syngas [2]. Subsequently, the exhaust anodic syngas can be combusted with depleted air from the cathodic stack section to enhance the overall system efficiency [3]. Furthermore, syngas or biogas renewable fuels are attractive for microreactors used for portable power generation [4,5].

Hybrid heterogeneous (catalytic) and homogeneous (gaseous) combustion approaches with syngas fuels are being investigated for large power plants [6–8]. These methods mitigate the risk of flashback (arising from the very reactive H_2 component) and appreciably reduce NOx emissions [9]. The most active catalyst for methane oxidation is palladium and, because of fuel-flexibility reasons, it is the favored catalyst when using either natural gas or syngas fuels. The oxidation of methane and syngas over palladium at high temperatures (> 800 K) relevant to large power plants has been studied in [10,11]. Therein, controlling process is the decomposition of the active PdO above ~1050 K (at atmospheric pressure in air) to the less active metallic Pd, which creates a strong hysteresis in the fuel consumption during sequential heating and cooling cycles [12].

Low-to-moderate temperature (500 to 800 K) oxidation of syngas in air, typically occurring on the PdO phase, is important for understanding the key ignition (light-off) processes in power systems. Past studies of low-temperature syngas oxidation on Pt, Pd and Rh [13–17] have exposed complex chemical interactions between CO and H_2, manifested by the presence of specific temperature windows where one fuel component may inhibit or promote the oxidation of the other [15–17]. The foregoing H_2/CO kinetic interaction studies on noble metals have been conducted at a given pressure, such that the impact of varying pressure has not been elaborated. Our past work investigated such interactions at atmospheric pressure and led to the development of a suitable catalytic reaction mechanism for the oxidation of lean syngas/air mixtures over PdO [17]. However, elevated pressures are of prime interest for both large-scale and portable power generation [7,18,19] and H_2/CO kinetic interactions have not been previously investigated at such conditions.

The current work investigates the combustion of fuel-lean H_2/CO/O_2/N_2 mixtures over PdO at pressures 3 to 10 bar, H_2:CO molar ratios of 1:5 to 3:1 and catalyst temperatures 540 to 690 K. In situ Raman measurements of the major gas-phase species concentrations across a channel-flow reactor monitored the catalytic processes [20], while 2D simulations were performed using detailed heterogeneous chemistry. The main objectives are to investigate first the high-pressure combustion of the individual fuel components and subsequently assess the kinetic coupling of H_2 and CO, to delineate the parameter space wherein H_2 inhibits the oxidation of CO and to draw implications of these findings to syngas-fired catalytic burners of power systems.

2. Experimental

2.1. Catalytic reactor and high-pressure test rig

The channel-flow reactor comprised two 9-mm-thick horizontal ceramic plates made of Si[SiC] (having length (-x), width (-z) and separation (-y) of 300 mm, 104 mm and 7 mm, respectively) and two 5-mm-thick vertical quartz windows (see Fig. 1 and details in [16,21]). The reactor was affixed in an insulated Inconel frame and the integrated assembly was positioned inside a high-pressure cylindrical steel vessel with an internal diameter of 26 cm

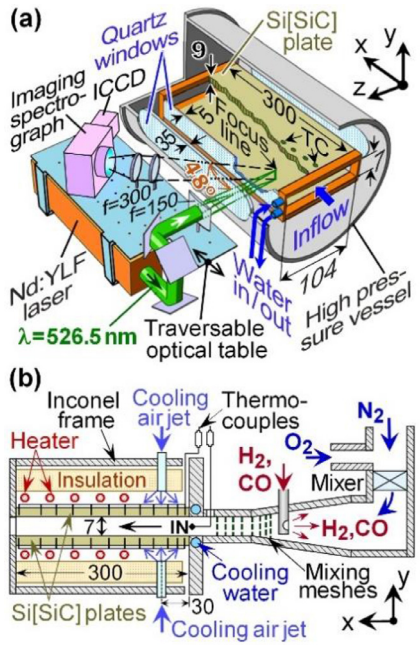

Fig. 1. (a) Test rig and Raman optical setup, (b) reactor details (lengths in mm).

(Fig. 1a). Optical access to both 300×7 mm^2 reactor sides was facilitated by two 350-mm-long and 35-mm-thick quartz windows on the vessel (Fig. 1a). The surface temperatures were monitored by 12 (for each plate) S-type thermocouples, situated along the x-y symmetry plane and fixed 0.9 mm beneath the catalyst through 1.2-mm-diameter and 8.1-mm-deep holes eroded from the outside Si[SiC] surfaces.

The inside surfaces of the Si[SiC] plates were coated by means of Plasma Vapor Deposition (PVD) with a 1.5 μm thick non-porous Al_2O_3 layer and then with a 2.2 μm thick palladium layer. The considerably thick palladium layer resembled a polycrystalline surface [11], while X-ray photoelectron spectroscopy (XPS) analysis carried out in the present work verified the absence of Al or Si from the catalyst surface.

Attaining modest catalyst temperatures (< 690 K) at the considerably exothermic syngas equivalence ratios $\varphi = 0.13$ and 0.23 was quite demanding; this was further compounded by the low Lewis number of H_2 ($Le_{H2} \sim 0.3$) that resulted in superadiabatic surface temperatures [22,23]. Consequently, an adjustable cooling power system was designed to control the surface temperatures. For the front Si[SiC] faces (110×9 mm^2), a water circuit in the Inconel frame (Fig. 1a) produced a base-level cooling power. The total cooling power was finely controlled by two room-temperature air jets with adjustable flows, impinging on the outside Si[SiC] surfaces, at $x = 30$ mm (Fig. 1b). Despite the jet-air and water cooling of the Si[SiC] upstream section, the downstream part ($100 < x < 300$ mm) had to be heated with two resistive coils, to counteract heat losses to the Inconel frame that could in turn extinguish catalytic reactions over the full reactor length.

Batteries provided H_2, CO, N_2 and O_2, with four Brooks mass flow meters regulating the gas flowrates. H_2/CO premixtures were injected counterflow to the O_2/N_2 premixtures, and final mixing of the two steams was achieved in a 200-mm-long steel conical unit (Fig. 1b). Good mixing and uniform exit velocities were obtained and confirmed (details in [16,21]). A K-type sheathed thermocouple, marked "IN" in Fig. 1b measured the inlet ($x = 0$) gas temperature.

2.2. Laser diagnostics

Excitation for the Raman measurements was achieved by a frequency-doubled Nd:YLF laser beam at 526.5 nm (Quantronix Darwin-Duo 80, 2 kHz repetition rate, pulse energy and duration of 40 mJ and 120 ns, respectively). The beam was focused by an $f = 150$ mm cylindrical lens into a 0.3-mm-thick vertical line, which encompassed the 7 mm channel height (Fig. 1a). The focus was offset 15 mm (in -z) from the x-y symmetry plane, to enhance the signal collection angle and diminish thermal beam steering (as in [17,24]). The collecting optics included two spherical lenses ($f = 300$ mm, f/4) that focused the scattered light into a 25 cm spectrograph (Chromex-250i) supplied with an ICCD camera (Princeton-Instruments PI-MAX1024GIII, 640×255 pixels, pertaining to spectral shift and y-distance, respectively). The 7 mm channel height was resolved with 220 pixels, which were subsequently binned to 64 pixels.

A tilted holographic notch filter (Kaiser-Optical-Systems 532 nm) and a glass filter (OG550 Schott) in front of the ICCD lens suppressed interferences from the excitation beam. A traversable optical table housed all optics (including the Nd:YLF laser and the spectrograph), while the 48° angle between the sending and collecting optical paths (Fig. 1a) allowed Raman measurements over the extent $8 \le x \le 140$ mm. Since all experiments were performed at steady conditions, scattered light from 180,000 to 360,000 laser pulses (increasing number with decreasing pressure) was integrated on the detector chip to increase the signal-to-noise ratio. The effective Raman cross-sections were assessed by recording signals from pressurized CO, H_2, N_2 and O_2 and the actual reactive mixtures. For species with volumetric contents ≥ 3% the measurement accuracy was ±3%, whereas for volumetric contents down to 0.5% the accuracy dropped to ±8%; lower contents could not be effectively resolved. Owing to low signal-to-noise ratios, data closer than 0.5 to 0.7 mm from the catalytic walls were not considered.

3. Numerical

Two-dimensional simulations along the x-y symmetry plane were performed with a steady Navier-Stokes CFD code (details in [15,16]). Only the front half channel domain 150×7 mm^2 was simulated, as the key kinetic interactions occurred over the Raman measurement extent $x \le 139$ mm. 620×80 grid points (in -x and -y, respectively) yielded grid-independent solutions. The lower and upper wall ($y = 0$ and 7 mm, respectively) axial temperature profiles were prescribed, by fitting curves through the 12 wall thermocouple measurements. At the inlet ($x = 0$), all properties were uniform.

The detailed H_2/CO catalytic reaction mechanism on PdO developed in our earlier atmospheric-pressure study [17] was used (8 surface and 8 gaseous species, 25 reactions, surface site density 1.46×10^{-9} mol/cm^2). Surface temperatures were appreciably low (< 690 K) for gas-phase chemistry to be of importance, as verified by additional simulations with the inclusion of the Li et al. [25] syngas gas-phase mechanism. The reaction rates were computed by Chemkin [26,27], whereas a mixture-averaged transport model was employed with thermal diffusion for H and H_2 [28].

4. Results

Prior to each test, the reactor was heated to 673 K in air for 1 hr to ensure that the catalyst comprised PdO phase. This was confirmed by ex-situ XPS measurements on 10×10 mm^2 samples, either fresh at 293 K or heated to 673 K (representative mean value for the surface temperatures in the present study). The fresh unheated samples comprised metallic Pd (Fig. S1a). The 673 K samples were eventually cooled to room temperature and analyzed, revealing PdO phase. This was expected, as the decomposition of PdO to Pd at ambient air conditions occurs at ~1050 K, i.e. much higher than the present temperatures. The EDX in Fig. S1b corroborated the increased oxidation state of the heated sample. Finally, the SEM images in Fig. S1c indicated a change in surface morphology from a smooth polycrystalline structure in the fresh sample to an increased area in the heated sample - albeit without the pronounced surface porosity observed in [17] at significantly higher temperatures of ~1000 K.

Pressures 3 to 10 bar, H_2:CO volumetric ratios 1:5 to 3:1 and global equivalence ratios (based on both H_2 and CO) $\varphi = 0.13$ and 0.23 were investigated (see Table 1). Pure CO and H_2 fuels were also studied (group cases A-D). In all cases the inlet temperatures were practically the same ($T_{IN} = 300$-302 K), while for a given pressure the inlet velocities (U_{IN}) were constant. At $p = 3$ bar, $U_{IN} = 0.86$ m/s and at higher pressures the velocities were reduced according to $U_{IN,p} = [(p_o = 3 \text{ bar})/p]\times U_{IN,p=3}$ so as to keep the same inlet Reynolds number in each group of Table 1. Laminar flows were established, with inlet Reynolds numbers (based on the channel height) 980-1050.

The conditions in Table 1 are of interest in many practical systems. In particular, H_2:CO volumetric ratios 1:1 to 3:1 are used in synthesis-gas-based production of chemicals, while the highest ratio 3:1 is also employed in pre-combustion decarbonization gas-turbine concepts [1]. Low H_2:CO ratios down to 1:5 and pressures up to 10 bar are relevant to micro-gas-turbines when co-firing syngas with natural gas.

4.1. Combustion of single CO and H_2 fuels

The two fuel components were first investigated separately, to verify that the employed reaction mechanism captured their combustion characteristics. Predicted and measured transverse profiles of CO mole fractions for three different pressures and four selected axial positions are depicted in Fig. 2 (group cases A with $\varphi = 0.23$). Of the total 64 measurement points, up to 18 are plotted (for clarity) over the span $0.6 \lesssim y \lesssim 6.4$ mm that could be resolved experimentally. The measured axial wall temperature profiles are also shown in Fig. 2.

The computed CO mole fractions at both catalytic walls were well above zero for all cases and axial positions, indicating a kinetically-controlled CO conversion -which was in turn critical for kinetic validation. The measurements in Fig. 2 confirmed this behavior, despite the absence of Raman data within ~0.6 mm from both catalytic walls. The simulated CO profiles were in good agreement with the measurements at all pressures, reproducing the near-wall bending and hence the transverse gradients of the deficient reactant CO at the walls; these gradients were in turn directly related to the local CO catalytic reaction rates [20]. The simulations slightly overpredicted the catalytic reactivity, as the computed CO mole fractions at both walls were somewhat lower than the measurements. Similar behavior was also revealed for $\varphi = 0.13$ (see e.g. Fig. S2a). Comparisons of the CO profiles in Fig. 2 for the three different pressures and at the same x-positions, indicated an increase of the catalytic reactivity with rising pressure (manifested by the decreasing wall CO mole fractions with increasing pressure). Such direct comparisons were possible [29] since Cases A1-A4 had the same

Table 1
Experimental conditions[a].

Case	p	φ	H_2	H_2:CO
(A1, A2, A3, A4)	(3,5,8,10)	0.23	16.1 (CO)	0
(B1, B2, B3, B4)	(3,5,8,10)	0.13	11.5 (CO)	0
(C1, C2, C3, C4)	(3,5,8,10)	0.23	7.1	∞
(D1, D2, D3, D4)	(3,5,8,10)	0.13	6.2	∞
(E1, E2, E3, E4)	(3,5,8,10)	0.23	(9.2, 10.0, 10.6, 10.9)	3:1
(F1, F2, F3, F4)	(3,5,8,10)	0.23	(7.9, 8.7, 9.2, 9.5)	1.9:1
(G1, G2, G3, G4)	(3,5,8,10)	0.23	(7.1, 7.1, 7.3, 7.3)	1:1
(H1, H2, H3, H4)	(3,5,8,10)	0.23	(3.6, 3.6, 3.8, 3.9)	1:3
(I1, I2, I3, I4)	(3,5,8,10)	0.23	(2.6, 2.6, 2.7, 2.8)	1:5
(J1, J2, J3, J4)	(3,5,8,10)	0.13	(6.4, 7.1, 7.3, 7.3)	3:1
(K1, K2, K3, K4)	(3,5,8,10)	0.13	(5.5, 6.1, 6.4, 6.6)	1.9:1
(L1, L2, L3, L4)	(3,5,8,10)	0.13	(4.7, 4.7, 4.9, 5.1)	1:1
(M1, M2, M3, M4)	(3,5,8,10)	0.13	(2.4, 2.4, 2.5, 2.5)	1:3
(N1, N2, N3, N4)	(3,5,8,10)	0.13	(1.6, 1.6, 1.7, 1.8)	1:5

[a] Pressure (bar), equivalence ratio, H_2 (CO for groups A and B) vol. content (%), and H_2:CO vol. ratio.

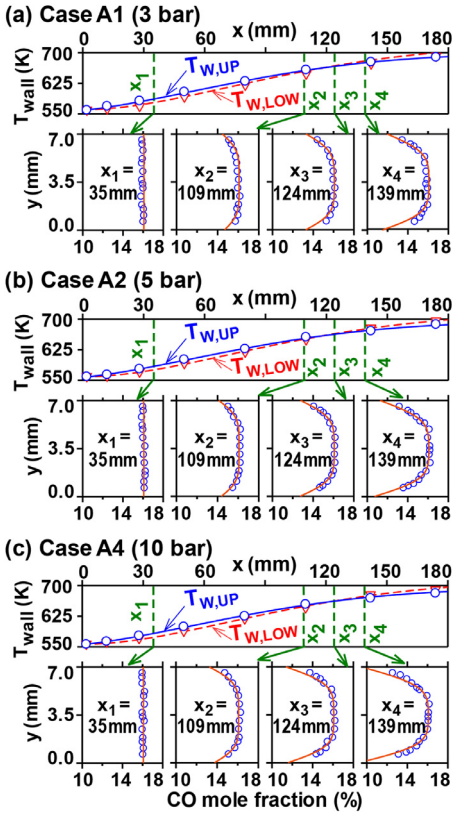

Fig. 2. (a) Case A1, (b) Case A2 and (c) Case A4. Top graphs: measured wall temperatures (symbols) and fitted profiles (lines). Bottom graphs: Raman-measured (symbols) and simulated (lines) y-profiles of CO mole fractions.

inlet Reynolds numbers and their wall temperatures were very similar (differed by less than 6 K over the axial extent of the measurements, see Fig. 2). Detailed simulations with the SPSR (Surface Perfectly Stirred Reactor) package of Chemkin [30] revealed that the pressure dependence of the CO reactivity was $\sim p^{0.74}$ (see analysis in Fig. S3a).

Results for H_2 are shown in Fig. 3 for $\varphi = 0.23$. Given the higher reactivity of H_2 compared to CO, up to 100 K lower wall temperatures were needed to ensure kinetically controlled H_2 conversions (see the temperatures in Figs. 2 and 3). Moreover, the upper and lower wall temperatures in Fig. 3 differed by up to 30 K, leading to more pronounced asymmetry in the profiles of H_2. There was again good agreement between measurements and simulations, with the latter modestly underpredicting the H_2 catalytic reactivity (for $\varphi = 0.13$, Fig. S2b shows a similar behavior). Comparisons of the H_2 profiles at the same x-location for the two pressures (given that in Cases C1 and C4 the corresponding upper/lower wall temperatures differed by less than 8 K and the inlet Reynolds numbers were the

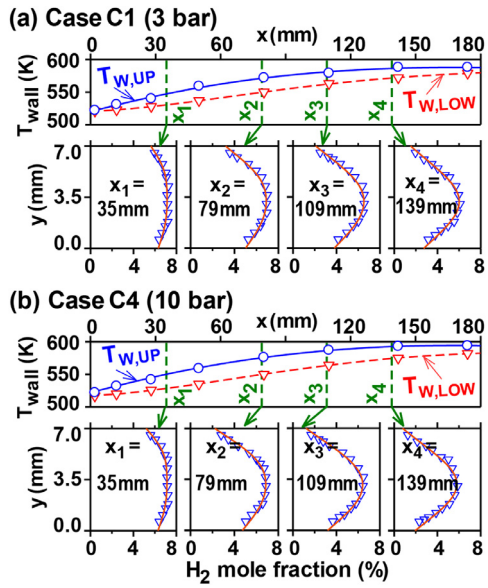

Fig. 3. Wall temperatures and y-profiles of H_2 mole fractions for (a) Case C1 and (b) Case C4. Notations as in Fig. 2.

same), indicated a very weak increase of the reactivity with rising pressure. SPSR simulations verified this, showing a $\sim p^{0.10}$ dependence of H_2 catalytic reactivity (see Fig. S3b). The deduced pressure exponents in Fig. S3 refer to the present $\varphi = 0.13$ and 0.23 and may not be suited for higher stoichiometries.

4.2. Combustion of H_2 and CO mixtures

Simulated and measured profiles of H_2 and CO mole fractions as well as measured wall temperatures are shown in Fig. 4 at four selected axial locations, for $p = 3$ bar, $\varphi = 0.23$ and three H_2:CO ratios. To unravel the interactions between H_2 and CO, further simulations are provided for the CO (dashed lines in Fig. 4(a1-a4, b1-b4, c1-c4)), which were obtained by replacing the H_2 in the syngas mixtures with an artificial species H_2^* that had the same transport and thermodynamic properties as H_2 but was chemically inert (did not participate in any reaction). Conversely, another set of simulations for H_2 was also carried out (dashed lines in Fig. 4(a5-a8, b5-b8, c5-c8)) by replacing CO in the syngas with an artificial species CO^* that had the same transport and thermodynamic properties as CO but was chemically inert. In the latter simulations, the dashed lines (with CO^*) practically coincided with the solid lines (with standard CO).

The measurements and the standard predictions (solid lines) for CO and H_2 were in good agreement with each other. At the first two positions in Fig. 4(a1-a2, b1-b2, c1-c2) the CO catalytic reactivity was minute, such that the abscissas were signif-

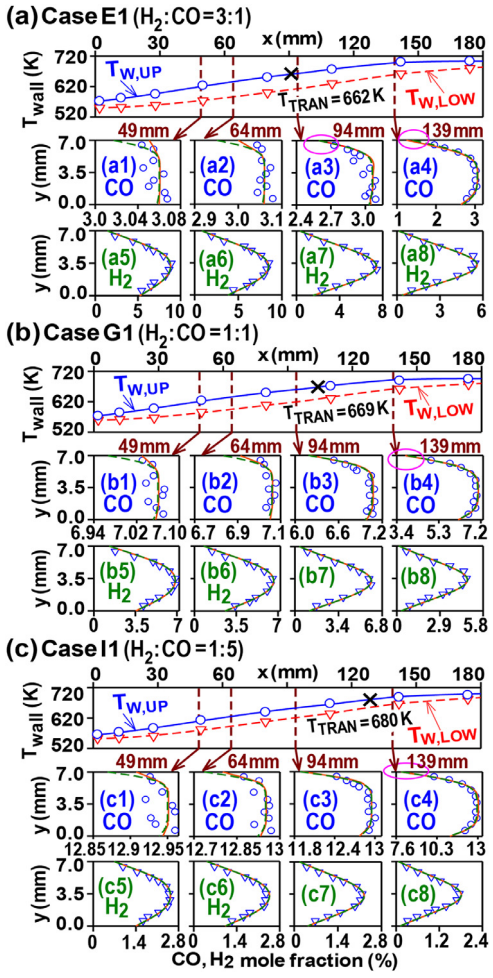

Fig. 4. (a) Case E1, (b) Case G1 and (c) Case I1, $p = 3$ bar and $\varphi = 0.23$. Top graphs: measured wall temperatures (symbols) with fitted profiles (lines). Middle and bottom graphs: Raman-measured (symbols) and predicted (solid lines) profiles of CO and H_2 mole fractions. Dashed lines in the CO plots denote predictions by replacing H_2 with an inert H_2^* species, whereas dashed lines in the H_2 plots denote predictions by replacing CO with an inert CO* species. Cross (×) symbols demarcate transition temperatures.

icantly stretched to expose the near-wall behavior. Evidently, on such a scale, there was a larger scatter in the Raman measurements due to the associated experimental uncertainties.

In summary, the comparison of experiments and simulations in Figs. 2, 3 and 4 attested the overall suitability of the employed kinetic mechanism for H_2/CO mixtures at pressures up to 10 bar. Comparisons of the standard CO/H_2 computations (solid lines) to CO computations with H_2^* (dashed lines), attested the existence of transition temperatures (T_{TRAN}) below which H_2 inhibited the

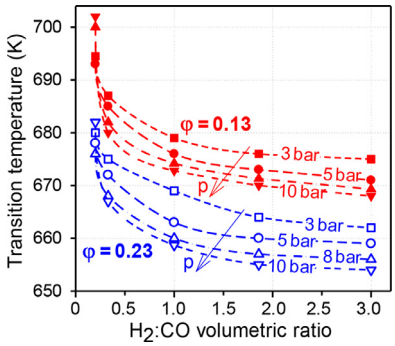

Fig. 5. Transition temperatures T_{TRAN} for all syngas cases in Table 1. Open symbols: $\varphi = 0.23$; filled symbols: $\varphi = 0.13$.

oxidation of CO. For example, at the upstream locations $x = 49$ mm and 64 mm in Fig. 4(a1, a2), the dashed lines indicated a higher reactivity of CO when using inert H_2^* (manifested by the lower CO mole fractions at the top wall and the steeper CO transverse wall gradients). However, at $x = 94$ mm and 139 mm in Fig. 4(a3, a4) the CO reactivity was higher in the standard simulations: therein, the CO mole fraction at the top wall computed with standard simulations overtook the CO computed with H_2^* (see circled areas at the top wall in Fig. 4(a3, a4)).

The precise transition temperatures were deduced from the simulations. For Case E1, $T_{TRAN} = 662$ K, occurring at $x_{TRAN} = 91$ mm (see cross symbol in the upper wall temperature profile of Fig. 4a). No transition was observed at the lower wall, as the temperatures there were always lower than T_{TRAN} over $x \leq 139$ mm. It is noted that the straightforward calculation of T_{TRAN} was enabled by the heating/cooling plate arrangement that always led to wall temperatures monotonically increasing with x. As the H_2:CO ratio decreased, T_{TRAN} increased (see Fig. 4(b, c)) such that $T_{TRAN} = 669$ K and 680 K for H_2:CO = 1:1 and 1:5, respectively. Furthermore, the standard simulations with CO and those with CO* in Fig. 4(a5-a8, b5-b8, c5-c8) provided virtually identical H_2 profiles, indicating a one-way kinetic coupling between H_2 and CO.

While the presence of H_2 inhibited CO oxidation at $T < T_{TRAN}$ and promoted CO oxidation at $T \geq T_{TRAN}$, the presence of CO had a practically neutral effect on H_2 oxidation over the investigated wall temperatures. This was in contrast to rhodium, where a strong two-way kinetic coupling between H_2 and CO oxidation was reported [16]. Similarly-computed T_{TRAN} at higher pressures and at $\varphi = 0.13$ are shown in Fig. S4(I) and S4(II), respectively. Finally, the T_{TRAN} for all syngas cases are summarized in Fig. 5. For a given pressure and φ, T_{TRAN} dropped monotonically with increasing

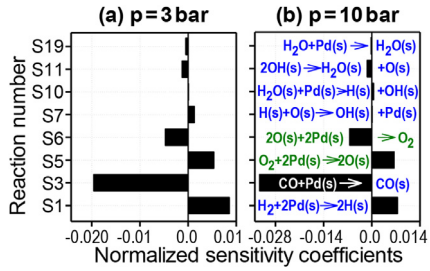

Fig. 6. Sensitivity analysis for CO in an SPSR, composition of Case E1, at (a) $p = 3$ bar, (b) $p = 10$ bar.

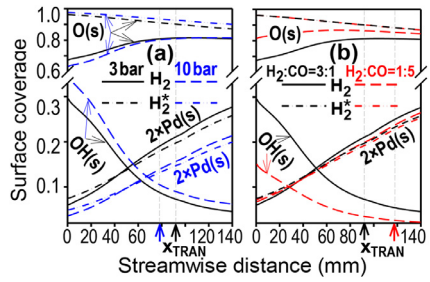

Fig. 7. Surface coverage at the top channel wall: (a) Case E1 (3 bar) and Case E4 (10 bar) at H_2:CO = 3:1, (b) Case E1 (H_2:CO = 3:1) and Case I1 (H_2:CO = 1:5) at $p = 3$ bar.

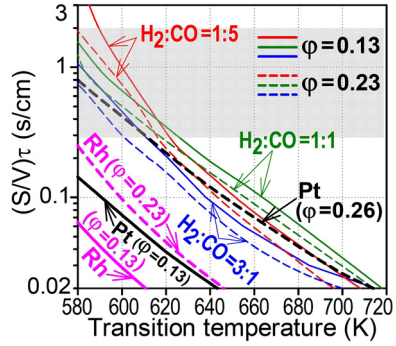

Fig. 8. Transition temperatures in an SPSR as function of the product of surface-to-volume ratio (S/V) and residence time τ. The thick lines correspond to earlier Pt [15] and Rh [16] results at H_2:CO = 1:1. The shaded area demarcates $(S/V)\tau$ regimes in power generation systems.

H_2:CO ratio. For a given φ and H_2:CO ratio, T_{TRAN} dropped monotonically with increasing pressure with an exception at the lowest H_2:CO = 1:5.

4.3. Kinetic coupling of H_2 and CO

The key reactions affecting CO conversion were identified with a sensitivity analysis, performed with SPSR simulations for the composition of Case E1, at 650 K ($< T_{TRAN}$, see Fig. 5). The sensitivity coefficients for CO are shown in Fig. 6; reactions with positive (negative) values increased (decreased) the CO amount in the SPSR and hence inhibited (promoted) CO consumption.

Main reactions were the adsorption of CO (S3, promoting), the adsorption of H_2 (S1, inhibiting) and the O_2 adsorption/desorption (S5/S6). Compared to the promoting effect of CO (S3), the inhibiting effects of H_2 (S1) and O_2 (S5) were proportionally stronger at 3 bar than at 10 bar. This is attributed to the stronger pressure exponent of the CO compared to the H_2 kinetics on PdO, as discussed in Section 4.1. Fig. 6 further shows that from the less significant reactions, the H(s)+O(s) → OH(s)+Pd(s) had the highest pressure sensitivity.

Case E1 was used as a nominal case to study the dependence of T_{TRAN} on pressure, H_2:CO ratio and φ. The coverage of the main surface species at the top wall of Case E1 is illustrated in Fig. 7. The effects of pressure and H_2:CO ratio were studied through Cases E4 and I1, with their main coverages plotted in Fig. 7a and 7b, respectively. To effectively decouple thermal from chemical effects, in the simulations of Cases E4 and I1 their wall temperatures were replaced by those of Case E1. The corresponding coverages for simulations with H_2*/CO are also included in Fig. 7.

The oxidation of CO was controlled by a complex interplay between the main O(s), OH(s) and Pd(s) coverages. In all cases, comparisons of H_2*/CO and H_2/CO simulations revealed that the latter always led to lower O(s) due to the creation of OH(s) (especially at upstream, lower-temperature positions). Moreover, Pd(s) was initially higher in the H_2*/CO simulations, shifting to lower after a certain distance $x < x_{TRAN}$. In Fig. 7b, the H_2:CO = 1:5 favored larger O(s) compared to H_2:CO = 3:1 and this in turn led to lower free sites Pd(s) for CO to adsorb for $x > 40$ mm. This could account for the increase of T_{TRAN} and x_{TRAN} with decreasing H_2:CO ratio. Conversely, an increase in pressure reduced both T_{TRAN} and x_{TRAN} (Fig. 7a). Even though a rise in pressure reduced the free sites Pd(s), this did not hamper the more efficient oxidation of CO (lower T_{TRAN}) as the catalytic reactivity of CO had a strong $\sim p^{0.74}$ dependence.

Further characterization of T_{TRAN} is presented in the SPSR simulations of Fig. 8, obtained with the compositions in Table 1 at 5 bar (this pressure allowed comparisons with past results on Pt [15] and Rh [16]). T_{TRAN} was controlled by the inlet composition and by the product of the reactor residence time (τ) and surface-to-volume ratio (S/V). This was because the SPSR gaseous species equations were $\rho(Y_{k,IN} - Y_{k,OUT}) = (S/V)\tau\ \dot{s}_k W_k$, with Y_k, $\dot{s}_k$ and W_k the mass fraction, molar catalytic reaction rate and molecular weight of species k, respectively, and ρ the mixture density. For a fixed (S/V) τ, T_{TRAN} was computed by gradually decreasing the SPSR temperature and determin-

ing the lowest possible temperature for which the CO conversion with H_2/CO mixtures exceeded the conversion with H_2*/CO mixtures. The computed T_{TRAN} decreased monotonically with increasing $(S/V)\tau$, whereas for a fixed $(S/V)\tau$ the T_{TRAN} generally decreased with increasing H_2:CO ratio and increasing φ.

In power generation gas-turbine catalytic burners [10], the product $(S/V)\tau$ is typically ~0.3-2.0 s/cm (shaded area in Fig. 8). In this industrially-relevant $(S/V)\tau$ range, temperatures 580-620 K were required to eliminate the H_2 inhibition on CO oxidation over PdO. Results for Rh ($\varphi = 0.13, 0.23$) and Pt ($\varphi = 0.13, 0.26$) at H_2:CO = 1:1 are also included in Fig. 8. Contrary to PdO, Pt and Rh had lower transition temperatures at lower φ. Moreover, the T_{TRAN} were lower on Pt, and especially on Rh, when compared to PdO. This suggested that Pt and Rh were more suited for the combustion of syngas in practical devices. On the other hand, the H_2 and CO coupling was weaker on PdO compared to Rh and Pt. For example, below the transition temperature the conversion of CO was only moderately inhibited by H_2 (see e.g. CO profiles in Fig. 4(a1-a3, b1-b3, c1-c3)), whereas the corresponding CO inhibition by H_2 on Pt and Rh was stronger [15,16]. The implications were that a calculation of syngas ignition temperatures based solely on the less reactive component CO would only be moderately different from the ignition temperatures of H_2/CO mixtures having the same CO volumetric content. This, however, would not be the case for Pt and Rh. Hence, the design of syngas catalytic reactors based on Pt and Rh requires more complex ignition considerations compared to PdO.

5. Conclusions

The kinetic coupling between H_2 and CO during syngas combustion over PdO was studied at pressures 3 to 10 bar, H_2:CO volumetric ratios 1:5 to 3:1, equivalence ratios $\varphi = 0.13$ and 0.23, and surface temperatures 540 to 690 K. In situ Raman measurements yielded the major gas-phase species concentrations over the catalyst boundary layers and thermocouples monitored the surface temperatures. Simulations and measurements of the combustion of the single fuel components attested pressure dependencies of $p^{0.74}$ and $p^{0.10}$ for the catalytic reactivity of CO and H_2, respectively. Ex situ surface XPS measurements identified PdO as the active catalytic phase.

Comparison of simulations and measurements for the combustion of single H_2 and CO fuels as well as H_2/CO mixtures attested the aptness of the employed detailed catalytic reaction mechanism. Transition temperatures (T_{TRAN}) were determined below (above) which H_2 inhibited (promoted) the oxidation of CO. T_{TRAN} decreased (i.e. the inhibiting effect of H_2 was reduced) with increasing H_2:CO vol. ratio, increasing pressure and increasing equivalence ratio. Sensitivity analysis identified that the H_2 adsorption and O_2 adsorption reactions had the larger inhibiting effect on CO, especially at lower pressures.

The deduced kinetic interactions pointed to the advantage of high H_2:CO vol. ratio fuels (e.g. those created by an effective fuel decarbonization in IGCC power plants) and high pressures when using burners with PdO. Comparisons with similar kinetic studies on Pt and Rh indicated that their corresponding T_{TRAN} were lower than those of PdO. While this suggested that Pt and Rh were more favorable catalysts for the combustion of syngas in practical burners, the H_2 and CO coupling was nonetheless weaker on PdO at $T < T_{TRAN}$, thus potentially favoring also PdO for low-temperature syngas oxidation.

Declaration of Competing Interest

The authors declare that they have no known competing financial interests or personal relationships that could have appeared to influence the work reported in this paper.

Acknowledgements

Support was provided by the Swiss National Science Foundation (SNSF) under project 200021_179019. We thank Mr. Juergen Theile for the aid in the experiments and Drs. Mario El Kazzi and Erich De Boni for the surface science measurements.

Supplementary materials

Supplementary material associated with this article can be found, in the online version, at doi:10.1016/j.proci.2022.06.010.

References

[1] L.O. Nord, R. Anantharaman, O. Bolland, *Int. J. Greenh. Gas Control* 3 (2009) 385–392.
[2] T.G. Ghang, S.M. Lee, K.Y. Ahn, Y. Kim, *Int. J. Hydrog. Energy* 37 (2012) 3234–3241.
[3] S.A. Kashmiri, M.W. Tahir, U. Afzal, *Energies* 13 (2020) 5186.
[4] N.S. Kaisare, D.G. Vlachos, *Prog. Energy Combust. Sci.* 38 (2012) 321–359.
[5] R. Sui, E.T. Es-sebbar, J. Mantzaras, N.I. Prasianakis, *Combust. Sci. Technol.* 190 (2018) 336–362.
[6] J. Mantzaras, *Combust. Sci. Technol.* 180 (2008) 1137–1168.
[7] L.L. Smith, H. Karim, M.J. Castaldi, S. Etemad, W.C. Pfefferle, *Catal. Today* 117 (2006) 438–446.

[8] F. Bolaños-Chaverri, J. Mantzaras, T. Griffin, R. Bombach, D. Winkler, *Proc. Combust. Inst.* 38 (2021) 5443–5451.
[9] A. Schlegel, S. Buser, P. Benz, H. Bockhorn, F. Mauss, *Proc. Combust. Inst.* 25 (1994) 1019–1026.
[10] T. Griffin, W. Weisenstein, V. Scherer, M. Fowles, *Combust. Flame* 101 (1995) 81–90.
[11] R. Sui, J. Mantzaras, C.K. Law, R. Bombach, M. Khatoonabadi, *Proc. Combust. Inst.* 38 (2021) 6583–6591.
[12] J.G. McCarty, *Catal. Today* 26 (1995) 283–293.
[13] J.A. Federici, D.G. Vlachos, *Combust. Flame* 158 (2011) 2540–2543.
[14] C. Stewart, E.K. Gibson, K. Morgan, et al., *ACS Catal* 8 (2018) 8255–8262.
[15] X. Zheng, J. Mantzaras, R. Bombach, *Combust. Flame* 161 (2014) 332–346.
[16] R Sui, J Mantzaras, R Bombach, *Combust. Flame* 202 (2019) 292–302.
[17] R. Sui, W. Liang, L. Zhang, J. Mantzaras, C.K. Law, *Combust. Flame* 211 (2020) 270–280.
[18] F. Bolaños, D. Winkler, F. Piringer, T. Griffin, R. Bombach, J. Mantzaras, Study of a rich/lean staged combustion concept for hydrogen at gas turbine relevant conditions GT2013-94420, ASME Turbo Expo, 2013, *Turbine Technical Conference and Exposition*, 2013.
[19] S. Karagiannidis, K. Marketos, J. Mantzaras, R. Schaeren, K. Boulouchos, *Catal. Today* 155 (2010) 108–115.
[20] J. Mantzaras, *Prog. Energy Combust. Sci.* 70 (2019) 169–211.
[21] R. Sui, E.T. Es-Sebbar, J. Mantzaras, R. Bombach, *Combust. Flame* 180 (2017) 184–195.
[22] J. Mantzaras, Catalytic combustion of hydrogen, challenges, and opportunities A.G. Dixon (Ed.), Modeling and Simulation of Heterogeneous Catalytic Processes, Advances in Chemical Engineering, 45, Elsevier Academic Press Inc, San Diego, USA, 2014.
[23] W.C. Pfefferle, L.D. Pfefferle, *Prog. Energy Combust. Sci.* 12 (1986) 25–41.
[24] R. Sui, J. Mantzaras, E.T. Es-sebbar, R. Bombach, *Proc. Combust. Inst.* 37 (2019) 5465–5472.
[25] J. Li, Z.W. Zhao, A. Kazakov, M. Chaos, F.L. Dryer, J.J. Scire, *Int. J. Chem. Kinet.* 39 (2007) 109–136.
[26] M.E. Coltrin, R.J. Kee, F.M. Rupley, *Surface Chemkin: A Fortran Package For Analyzing Heterogeneous Chemical Kinetics At the Solid Surface-Gas Phase interface, Report No. SAND90-8003C*, Sandia National Laboratories, USA, 1996.
[27] R.J. Kee, F.M. Rupley, J.A. Miller, *Chemkin II: A Fortran Chemical Kinetics Package For the Analysis of Gas-Phase Chemical kinetics, Report No. SAND89-8009B*, Sandia National Laboratories, USA, 1996.
[28] R.J. Kee, G. Dixon-Lewis, J. Warnatz, M.E. Coltrin, J.A. Miller, *A Fortran computer Code Package For the Evaluation of Gas-Phase Multicomponent Transport properties, Report No. SAND86-8246*, Sandia National Laboratories, USA, 1996.
[29] J. Mantzaras, C. Appel, *Combust. Flame* 130 (2002) 336–351.
[30] H.K. Moffat, R.J. Kee, J.F. Grcar, J.A. Miller, *Surface PSR: A Fortran Program For Modeling Well–Stirred Reactors With Gas and Surface reactions, Report No. SAND91-8001*, Sandia National Laboratories, USA, 1993.